A synthetic communication system uncovers self-jamming of bacteriophage transmission

Authors

Amit Pathania[1], Corbin Hopper[1,2,3], Amir Pandi[1], Matthias Függer[2]*, Thomas Nowak[3]*, Manish Kushwaha[1]*

[1] Université Paris-Saclay, INRAe, AgroParisTech, Micalis Institute, 78352 Jouy-en-Josas, France.
[2] Université Paris-Saclay, CNRS, ENS Paris-Saclay, Laboratoire Méthodes Formelles, Inria, 91190 Gif-sur-Yvette, France.
[3] Université Paris-Saclay, CNRS, Laboratoire Interdisciplinaire des Sciences du Numérique, 91405 Orsay, France.

*To whom correspondence should be addressed: mfuegger@lsv.fr, thomas.nowak@lri.fr, or manish.kushwaha@inrae.fr

Abstract

Intercellular communication enables coordinated action by cells of microbial communities and multicellular organisms, often mediated by molecular exchange of information. Inspired by their success, synthetic biologists have recently started implementing population-level controls in engineered organisms with the aim of expanding circuit size and complexity. Yet, realising the true potential of multicellular synthetic biology requires an expanded communication alphabet as well as quantitative models to predict complex behaviour. Towards that aim, here we repurpose the M13 bacteriophage machinery for cell-to-cell communication between *Escherichia coli* cells and characterise the signalling dynamics. The fitted quantitative model includes the growth burden of the communication machinery, the relationship between cellular growth phase and the secretion-infection kinetics, and concurrent antibiotic selection. Limitations of deterministic models are demonstrated, with stochastic effects playing a key role in reproducing the observed infection kinetics. Surprisingly, we discover that the M13 minor coat protein pIII is released into the medium to confer extracellular immunity to uninfected cells. In a simulated gut environment, this mechanism enables the phage to farm uninfected bacterial cells for the future, increasing the overall success of both M13 and *E. coli*. In addition to establishing a tool for intercellular communication, our work uncovers the mutualistic nature of a phage-bacterial relationship that has evolved over long-term coexistence.

Introduction

Intercellular communication is essential for coordination between cells in multicellular organisms and communities[1,2]. As the complexity of functions increases in biological systems, temporal and spatial division of labour emerge, the former by differential gene expression to generate phenotypic diversity and the latter by distribution of functions into specialised compartments, differentiated cell-types, and multicellular systems[2–5]. Most intercellular communication occurs via small molecules (metabolites, hormones, ions) exchanged through cell-to-cell contact or diffused through the intercellular space[6]. Communication may also occur via genetic information, in the form of RNAs, exchanged through cell junctions or packaged vesicles[7,8]. However, the largest throughput of information communication between cells, albeit over longer time-scales, takes place through genetic exchanges by horizontal gene transfer (HGT)[9]. Mediated by conjugation, transformation, or transduction, HGT is responsible for communicating genetic information from one cell to another, of the same or of a different species. By transferring genetic functions between organisms, HGT helps shape biological diversity throughout the tree of life[9], in natural and artificial ecosystems alike[10]. The functions communicated by HGT have a wide range, from antibiotic to heavy-metal resistance[11–13], carbohydrate metabolism to bioremediation[14,15], and virulence to immune escape[16,17]. Consequently, HGT facilitates an ecosystem-level division of labour between constituents of the multicellular communities[18].

In the past two decades of synthetic biology, remarkable progress has been made in the engineering of biological circuits that respond to external signals communicated to the cell for further processing and response[19–22], leading to a wide variety of applications from the detection of pollutants[23] and disease biomarkers[24] to the deployment of smart therapeutics[25,26]. Yet, most of these applications have relied on unicellular circuitry. With the aim of expanding circuit size and inspired by the distribution of biological functions in nature, approaches that decompose synthetic genetic circuitry into multiple cells have been proposed[27–29]. These enable new circuits to be generated in multicellular consortia by co-culturing cells containing the appropriate sub-circuits[28]. However, scaling up the distributed approach for multi-layered biological circuits requires that cells communicate with each other using orthogonal signals. Small molecules like homoserine lactone (HSL), repurposed from bacterial quorum sensing systems, and yeast pheromones have been used for diffusible signal communication between cells[27,28], and synthetic surface receptor-ligand pairs have been used for mammalian cell-to-cell communication[30]. Despite these developments, the available orthogonal communication alphabet of four HSLs[31], two pheromones[28], or two receptor-ligand pairs[30], remains severely limiting for higher-order multicellular circuits, both in orthogonality and information content.

An alternative to the limited communication alphabet of available small molecules is to use an information-rich, robust, and readily-programmable molecule like DNA for signal transduction in multicellular systems. In fact, DNA signals have already been employed for biological computing reactions implemented *in vitro* in one or more compartments[32,33]. DNA messages have the advantage of not only high information content but also huge potential for the systematic construction of orthogonal signals. Furthermore, they can self-execute upon delivery, conferring on their receiver cells new functions like biofilm formation or toxin production[17,34,35]. Promisingly, DNA-based communication has already been implemented in a few engineered examples[35,36], including in directed evolution systems that rely on exchange of DNA messages between cells in continuous cultures[37,38]. These examples have

employed conjugation for contact-transfer of DNA between cells[35], or a filamentous bacteriophage for transfer of the DNA message from the donor to the recipient[36–38]. As a highly abundant and extensively studied *E. coli* phage with widespread application in phage-display technologies[39], the non-lytic M13 phage is an ideal choice for repurposing as a synthetic messaging vehicle.

Here, we repurpose and characterise a phage-based synthetic intercellular communication system by relying on components commonly used in the M13 phage-display technology[40]. Sender cells carry DNA messages as phagemids, which contain the M13 packaging signal (PS)[41] for message secretion, and the M13 helper plasmid that encodes the functional protein machinery but no PS. Cells containing both these components secrete messages as packaged M13 phages. These messages can then infect receiver cells carrying the F-plasmid, which encodes the F-pilus receptor required for efficient M13 entry[40,42]. In a stepwise manner, we build, parameterise, and integrate realistic quantitative models of the communication system, performing a series of experiments to collect data on cell growth kinetics, phage secretion, and infection. Our model captures the growth burden of maintaining the communication machinery, the relationship between cellular growth phase and the sending and receiving kinetics of phage signals, as well as the effect of antibiotic resistance. We find that stochastic models of the communication system are key to predicting experimental outcomes from low-frequency infection events, as opposed to deterministic models. When using conditioned media to study the effect of nutrient depletion in long-term experiments, we surprisingly found a significant reduction in communication rates. Further investigation led us to uncover a self-jamming mechanism by which extracellular M13 minor coat protein pIII prevents uninfected cells from receiving the available phage signals. Model predictions show that the self-jamming mechanism confers an advantage to both M13 and *E. coli* in a simulated gut environment.

Results

Effect of cell physiology on phage secretion and infection rates

To measure the rate of M13 phage secretion from growing cells, senders (TOP10_H_KanΦ, Table S1, Fig. 1a) were grown over ~15 hours (Methods), with regular monitoring of their OD_{600} at 1h intervals (Fig. 1b), and fitted to a two-phase growth model based on Chemical Reaction Networks (Box S3, Notes S2 and S3). Briefly, growth of the bacterial cell (C) is represented as duplication reactions $C + R_i \rightarrow C + C$, where R_i is the phase-dependent nutritional resource consumed per duplication event. The phage samples, collected at the same time-points (Fig. 1c), were quantified using the CFU assay (Methods). Phage secretion decreases after 12h, consistent with previous observations of reduced filamentous phage secretion rates late in the infected state[40,43].

To model secretion of phages by sender cells, we differentiated the phage counts with respect to time and normalised the secretion rates by sender cell densities (Note S4). The resulting secreted phages min^{-1} $cell^{-1}$ is plotted in Fig. 1d (Note S4). To include the effect of sender physiology on secretion rates, we used a simple non-constant secretion model where the single-cell secretion rate is proportional to the cell growth rate and thus decreases with the depletion of resources. In our two-phase model, this is achieved by two phage secretion reactions, one per growth reaction, with rates proportional to the growth rates. The model prediction is shown in Fig. 1d. We estimate that phage secretion rates vary from 1

phage min^{-1} $cell^{-1}$ in the early phase to about 0.5 phage min^{-1} $cell^{-1}$ in the late phase (Fig. 1d-e). These numbers are lower than secretion rates reported for filamentous phages between 2.5 and 33.3 phages min^{-1} $cell^{-1}$ in the early phase of growth[43–45], raising the possibility that our phage secretion is less efficient than for WT M13 or that the CFU assay we use to determine phage counts underestimates the true viable phage counts in the medium. Comparisons of phage counting methods have previously found considerable variability in the reported numbers, depending on the assay method used[46] (Note S5).

We next set out to investigate the effect of receiver cells' (ER2738, Table S1, Fig. 1f) density and growth phase on the infection dynamics. While in a growing culture, cell density and growth phase change simultaneously, we designed our experiments to differentiate between the two effects (Fig. 1g-h). To determine the effect of receiver concentrations, they were grown to an OD_{600} ~1 (late log-phase), harvested, and resuspended to five different ODs, followed by infection with the same phage concentrations and subsequent plating on LB agar with kanamycin selection (Fig. 1g, Methods). As expected from mass-action kinetics, we found a positive relationship between receiver cell density and the number of colonies obtained on LB agar (Fig. 1i). To determine the effect of the receivers' growth phase, receivers were harvested at different growth phases, using OD_{600} of the growing cell culture as proxy, and resuspended to an OD_{600} of 0.5. As before, the resuspended receivers were infected with the same phage concentrations and plated on selective LB agar. We observed that the estimated phage numbers obtained from infected receivers were ~10- to ~35-fold higher when the receivers were harvested in the late growth phase as compared to the early growth phase (Fig. 1h). Since the OD_{600} of the receivers was the same in these experiments, the observed differences in colony counts are due to the differences in infectability of the receivers at different phases of growth, possibly because the number of F-pili per cell increases until the late log-phase[47]. Together, these results not only highlight the effect of receiver cell density and physiology on infection rates but also expose the limitations of the CFU method for estimating phage numbers (Note S5).

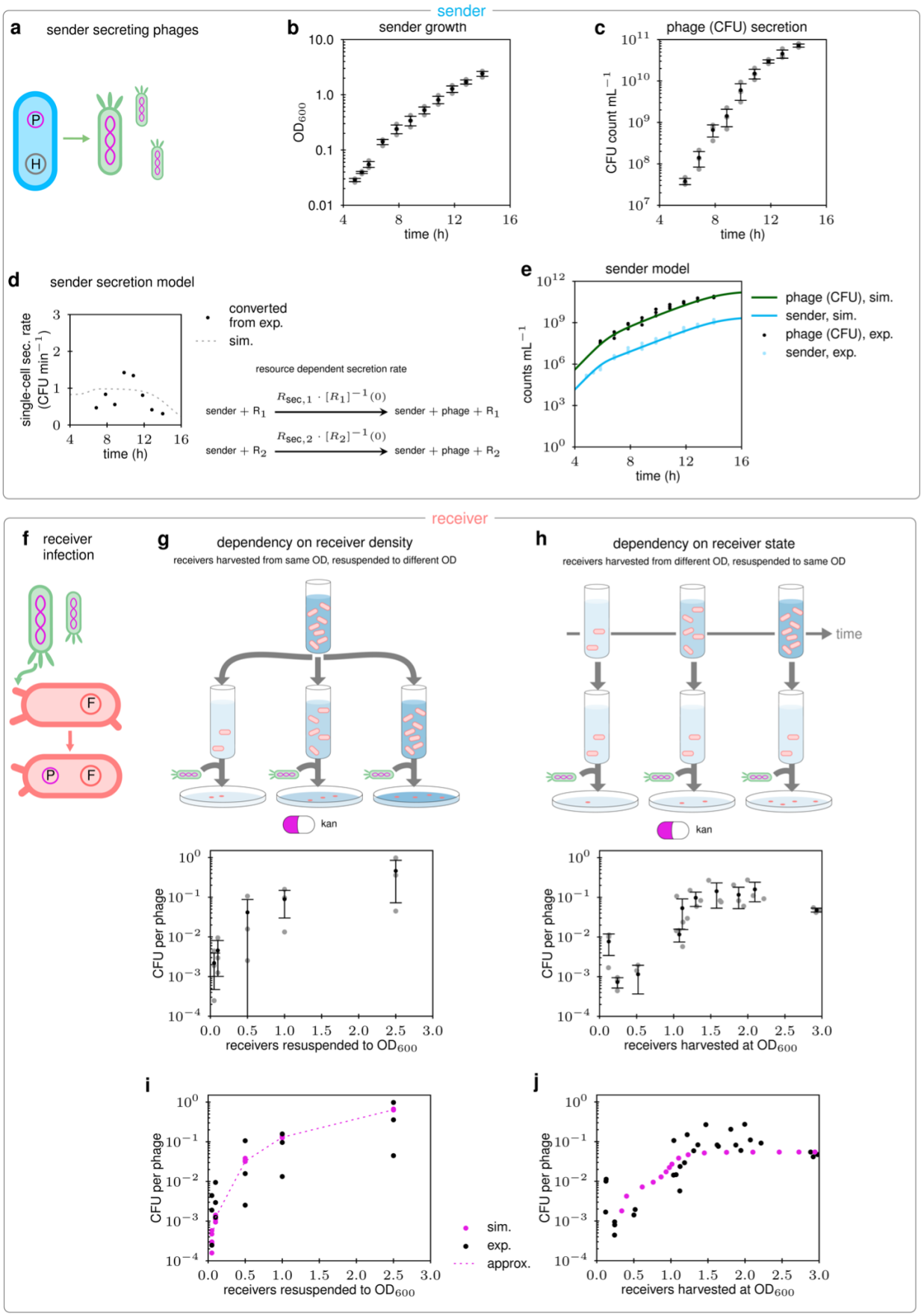

Fig. 1. Phage secretion and infection. (a) Characterisation of sender cells that carry a helper plasmid (H) and the phagemid (P). The latter is packaged into the secreted phage particles. **(b)** Senders were grown in a flask (in LB with antibiotics) after

inoculation with overnight cultures ($n = 3$ replicates, **Methods**). OD_{600} of the senders collected over time. Data (grey), and mean ± SD (black) are indicated. **(c)** Secreted phages were collected over time and the CFU assay was used to estimate their titres (**Methods**). Data (grey), and mean ± SD (black) are indicated. **(d)** The single-cell secretion rate in CFU min^{-1} computed from (b)+(c) is shown (black). The decrease over time was reproduced by resource dependent secretion reactions for R_1 and R_2. The resulting simulated single-cell secretion rate (grey dashed) reproduces the decay over time. **(e)** Blue: conversion of sender OD_{600} to counts mL^{-1} (**Note S2**) and fitting of a two-phase growth model to the timed data. Green = secreted phage concentrations in CFU mL^{-1} and simulation of a CRN sender model that integrates the two-phase growth and phage secretion (**Note S8**). exp. = experimental data & sim. = simulation. **(f)** Characterisation of receiver cells by infection assays. Receivers carry an F-plasmid (F) that encodes the formation of pili, the primary phage receptors. **(g)** The dependence of infection rates on receiver densities was determined by harvesting at OD_{600} ~1, re-dilution to different OD_{600}, and subsequent CFU assay ($n = 3$ replicates, **Methods**). The maximum CFU (at OD_{600} ~ 2.5) was taken as the phage count. Data (grey), and mean ± SD (black) are indicated. **(h)** The dependence of infection rates on the receiver state was determined by harvesting receivers at different OD_{600}, re-dilution to OD_{600} of 0.5, and subsequent CFU assay ($n = 6$ replicates over 2 days, **Methods**). Data (grey), and mean ± SD (black) are indicated. **(i)** Predictions of our receiver CRN model for the setup in (g) with stochastic simulations ($n = 6$ simulations per OD_{600}), as well as a deterministic simplified infection model (approx.) that does not consider bacterial growth (**Note S6**). Both predictions include the infection dynamics, in particular the increased infection rate for cells in later growth phases due to the increased ratio of highly infectable receivers. **(j)** Predictions of our receiver CRN model for the setup in (h). The stochastic model was used to simulate the growing receiver population, and determine the ratio of highly infectable receivers at different OD_{600}. Next, the deterministic simplified infection model (**Note S6**) was used to determine CFU concentrations (pink dots).

We modelled the relationship between receiver density and infection rates using mass-action kinetics (Note S8), running simulations with varying receiver densities. Using stochastic simulations (Fig. 1i, pink circles), we asked if the variance in the data (Fig. 1g) can be explained by the stochasticity of infection at small numbers. While the variance is pronounced at low OD_{600}, stochastic effects were found to be small overall. In fact, a deterministic simplified analytic infection model without bacterial growth, which is based on first-order infection kinetics (Note S6), is seen to approximate the stochastic simulations well (Fig 1i, pink dashed line). To model the higher infection rate for receivers in the late growth phase we introduced a new infectability state to the receiver model (Note S8). At the “low” infectability state, the receiver’s infection rate is only 0.4% of the “high” infectability state infection rate. We determined the rate constant of the high state infection reaction to be $3x10^{-10}$ mL min^{-1} from the experiments in Fig. 1g. In our model (Fig. 1j), daughter cells start at the low infectability state and transition to the high infectability state at a constant rate 0.25 h^{-1}. The distribution between low and high infectability states is determined by the initial distribution in the inoculated culture and the current OD_{600}.

Stochastic interactions influence infection dynamics of growing receiver cells

After analysing culture density and growth phase of receiver cells independently (Fig. 1), we investigated how infection rates change in a growing culture as their density and growth phase change simultaneously. We set up plate reader experiments with different combinations of 4 starting receiver cell densities and 12 phage concentrations (Fig. 2a, undiluted $8.16x10^5$ PFU mL^{-1} of pSB1K3_M13ps_LacZα_gIII phage, its fold dilutions 3^{-1} to 3^{-10}, and no phage control), and grew them over a duration of 20h with and without antibiotic selection (Fig. 2 and Fig. S8 to S11). In addition, we quantified unadsorbed phages from the 3^{-2} dilution at four time-points (Fig. 2c). We analysed the data to establish the killing curves due to antibiotic selection, and growth cost due to phage infection and maintenance.

Without antibiotic (kan) selection, phage concentrations do not substantially affect the growth trajectories of cultures (Fig. 2b). With antibiotic selection, receivers without phages gradually die, giving us the killing kinetics of kanamycin (Fig. 2g). However, phage infection can rescue cells from kanamycin-mediated killing, resulting in most of the kan(+) wells growing on the plate (Fig. 2d-f). When analysing the numbers of unadsorbed phages (Fig.

2c), we observe that in kan(-) wells phages continue getting adsorbed by growing cells until almost no phages are left by 6h. In the kan(+) wells ~50% of the phages get absorbed within the first 2h but this number remains unchanged afterwards. As seen in multiple experimental repeats, growth in kan(+) wells is very likely in the high phage & high cell density settings and very unlikely in the low phage & low cell density settings (Fig. S9). However, in the intermediate dilutions there is substantial variability observed across experimental repeats due to the probabilistic nature of contact between cells and phages (Fig. 2f).

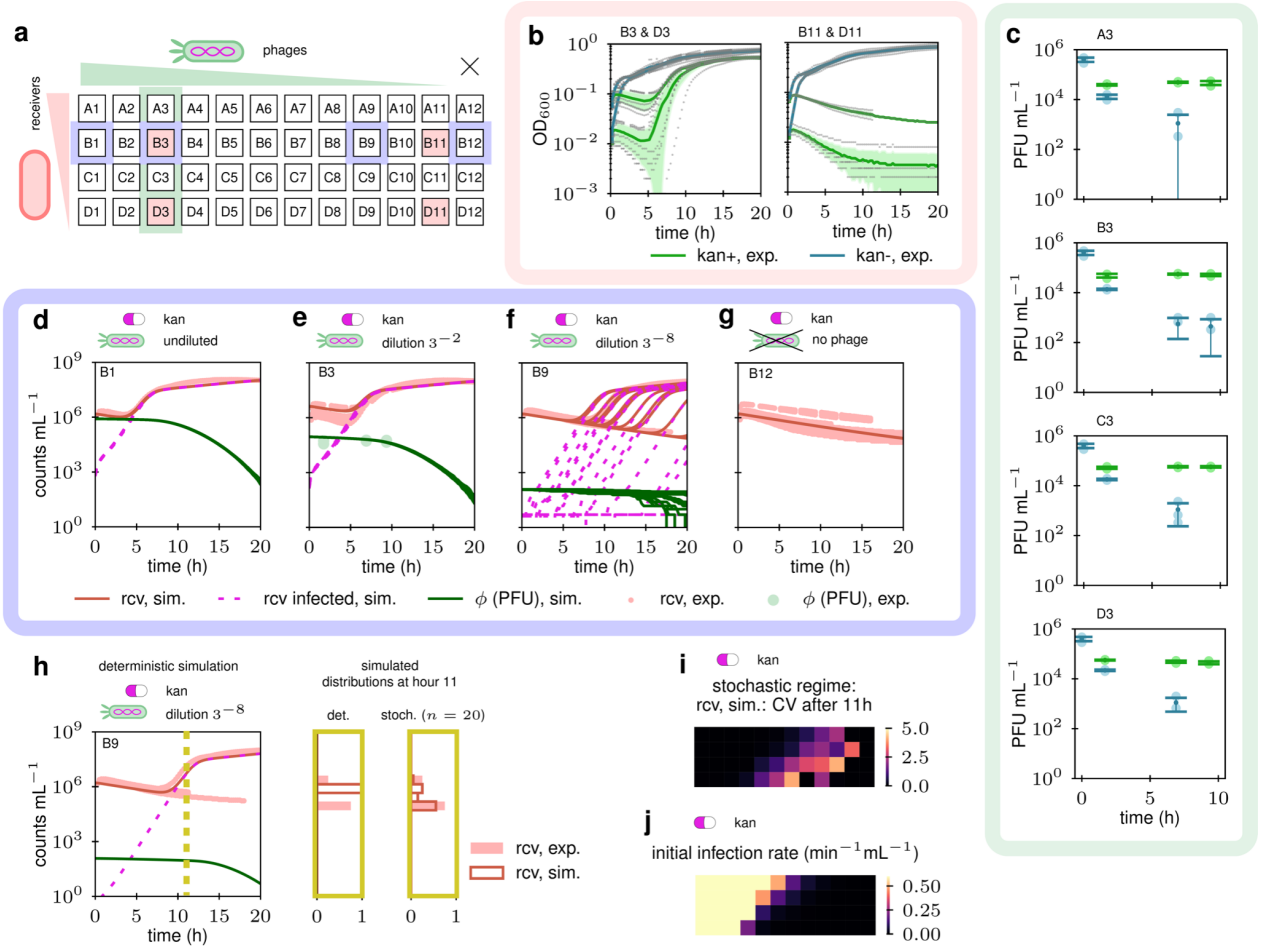

Fig. 2: Effect of phage reception by growing receiver cells. (a) To receivers at 4 different cell densities, phages with 12 different concentrations were added. The OD_{600} was varied (y-axis) from 0.25 (top, undiluted) in dilution steps of ½ until 0.03125 (bottom). Added phage concentrations were varied (x-axis) from undiluted (column 1), in dilution steps of ⅓ (columns 2-11). No phage was added to the rightmost column 12. Unadsorbed phage concentrations over time were measured by blue-plaque assays from the 3^{-2} dilution (column 3, **Methods**) **(b)** OD_{600} was measured over 20h in plate reader runs in the presence (green) and absence (blue) of kanamycin (details in **Fig. S9** and **S10**). Data (grey), mean (line) and standard deviation (shaded area) are indicated. **(c)** Unadsorbed phage concentrations (PFU mL^{-1}) over time for column 3 (n = 3) in the presence (green) and absence (blue) of kanamycin. Data (light circles), mean (dark circles) and SD (caps) are shown. **(d-g)** Converted receiver (rcv) cell densities (exp. = experimental data) and unadsorbed phages (ϕ (PFU)) are shown, together with stochastic simulations (sim. = simulation) of our receiver CRN model ($n = 20$ runs, **Note S8**) for varying initial phage concentrations in the presence of kanamycin. For the simulations, receivers (rcv), infected receivers (rcv infected), unbound phages in PFU (ϕ (PFU)) are shown. Plots for all wells, also in the absence of kanamycin, are shown in **Fig. S9** and **S10**. **(h)** Deterministic ODE simulation for the setting in (f). The two different experimental outcomes are visible and reproducible with the stochastic simulation in (f) but not with the deterministic simulation in (h). The distribution of receiver concentrations at hour 11 is shown in the yellow boxes for stochastic and deterministic simulations (rcv, sim), together with data from experiments (rcv, exp). Simulations and experiments match well in the stochastic case. **(i)** Heatmap of coefficient of variation (CV) of simulated ($n = 20$ runs) receiver concentrations at hour 11 in the presence of kanamycin. The layout of the heatmap is the same as for (a). A diagonal region with pronounced stochastic effects is clearly visible. **(j)** Heatmap of the initial infection rates (t = 0). Higher infection rates lead to likely infection and lower infection rates to likely absence of infection.

Since the phage confers antibiotic resistance against kanamycin, we included this effect in our mathematical model. We added a kanamycin species to the CRN model, which is consumed by the receiver cells during the reaction $K + C \rightarrow C'$, where C and C' denote the cell states before and after kanamycin uptake, respectively. A receiver cell that takes up kanamycin before phage infection dies with a rate proportional to its duplication rate resulting in higher killing rates for low initial receiver concentrations. Such a death rate fits our data well (Fig. 2g and S9), and is in agreement with previous observations that antibiotics that act via translation inhibition (like kanamycin) result in higher death rates for low initial *E. coli* concentrations[48]. To model the metabolic burden of phagemid maintenance after infection, we multiply each infected cell's duplication rate by a fitted penalty factor between 0 and 1 that increases from early to late growth phase (Note S8), which is consistent with fewer phages being produced during late infection[40,43]. A reduced infection rate by factor 0.3 for cells that had taken up kanamycin prior to infection was used (Note S8). Cells transition from the early to the late infection state at a constant rate of $1/3$ h^{-1} (Note S8). The model allows us to generate timed simulation traces involving infection and antibiotic killing-resistance kinetics. We used deterministic and stochastic simulations to predict OD_{600} trajectories across several experiments over 4 plate runs (Fig. 2d-g, S9, and S10).

While in the kan(-) plate reader experiments, deterministic simulations approximate stochastic simulations well (Fig. S10), this is not the case in the kan(+) experiments. The stochastic simulations (Fig. 2f) show that infected receivers (dashed) are low in number over a long period of time, and when they do grow there are large variations in the starting time depending on the initial receiver density. This results in large variations of the receiver concentrations after 5 hours, a behaviour that the stochastic simulations can reproduce (Fig. 2f), but the deterministic simulations cannot (Fig. 2h). The heatmap in Fig. 2i shows where stochastic simulations lead to large variations in receiver growth by reporting the coefficient of variation (CV) for receiver counts at hour 11. The darker top-left and bottom-right corners of the heatmap correspond to the setups where infection is either likely to occur or likely not to occur, following a deterministic pattern. The highest CV is seen along the diagonal where the lower numbers of phages or receivers result in high variability in infection outcomes. This can also be seen by considering the initial infection rates (Fig. 2j). The stochastic region corresponds to an expected first infection within the first few minutes, after kanamycin-mediated killing starts to significantly decrease the uninfected *E. coli* counts.

Communication between sender and receiver cells

We next studied the dynamics of intercellular communication between sender and receiver cells growing in a co-culture. To assess the communication between them via phages (pSB1K3_M13ps_LacZα_gIII), senders (TOP10_HΔgIII_gIII-KanΦ) and receivers (ER2738) grown to mid-log phase were mixed in combinations of different starting densities (OD_{600} of 0.136 and its dilutions by factor 2 per step). They were incubated without antibiotic selection for 1h (Fig. 3, Methods), following which they were grown in 4 experimental sets over 15h: one without antibiotics, and three with antibiotics to select for senders only (gentamycin), receivers only (tetracycline), or infected receivers only (kanamycin+tetracycline). OD_{600} measurements are shown in Fig. 3b-e and S18. To simulate these results, the sender secretion and receiver infection models were combined, and

effects of gentamycin and tetracycline selection added (Note S8). Experimental results and deterministic ODE simulations are shown in Fig. 3f-i, and S17 to S22. Stochastic simulations (data not shown) showed no apparent difference to the deterministic simulations.

In the absence of antibiotic selection, final ODs are lower when starting sender concentrations are high due to the senders growing slower than the receivers while consuming the resources (Fig. 3a-e, S19). This is confirmed by the model where senders dominate the final numbers in f and h (Fig. 3), but receivers dominate the numbers in g & i (Fig. 3). A similar effect is also observed when selecting for receivers, where higher starting sender concentrations lead to lower final ODs due to early resource competition before the senders are killed by the antibiotic (Fig. 3b-e), resulting in apparent biphasic growth at high starting sender concentrations. The model simulations confirm the overtaking of the dying senders by the receivers (Fig. S21). The reverse is observed when selecting for senders: final ODs are higher in wells with lower starting receiver concentrations (Fig. 3b&d), as confirmed by the model (Fig. S22). When selecting for infected receivers, the starting high-sender settings (Fig. 3b&d) show differences in growth due to the killing of senders and uninfected receivers, followed by the subsequent growth of infected receivers. These complex dynamics result in the observed biphasic growth curves that model simulations agree with (Fig. S23). The simulations explain the experimental data well (Fig. 3f-i, S18, S20 to S23), with a heatmap of the time taken to reach 10^6 infected receivers showing that starting high concentrations of both senders and receivers lead to faster infection rates (Fig. 3j). However, higher final infected receiver concentrations are achieved when starting with lower sender concentrations due to the lower starting competition facilitating later post-infection growth (Fig. 3k).

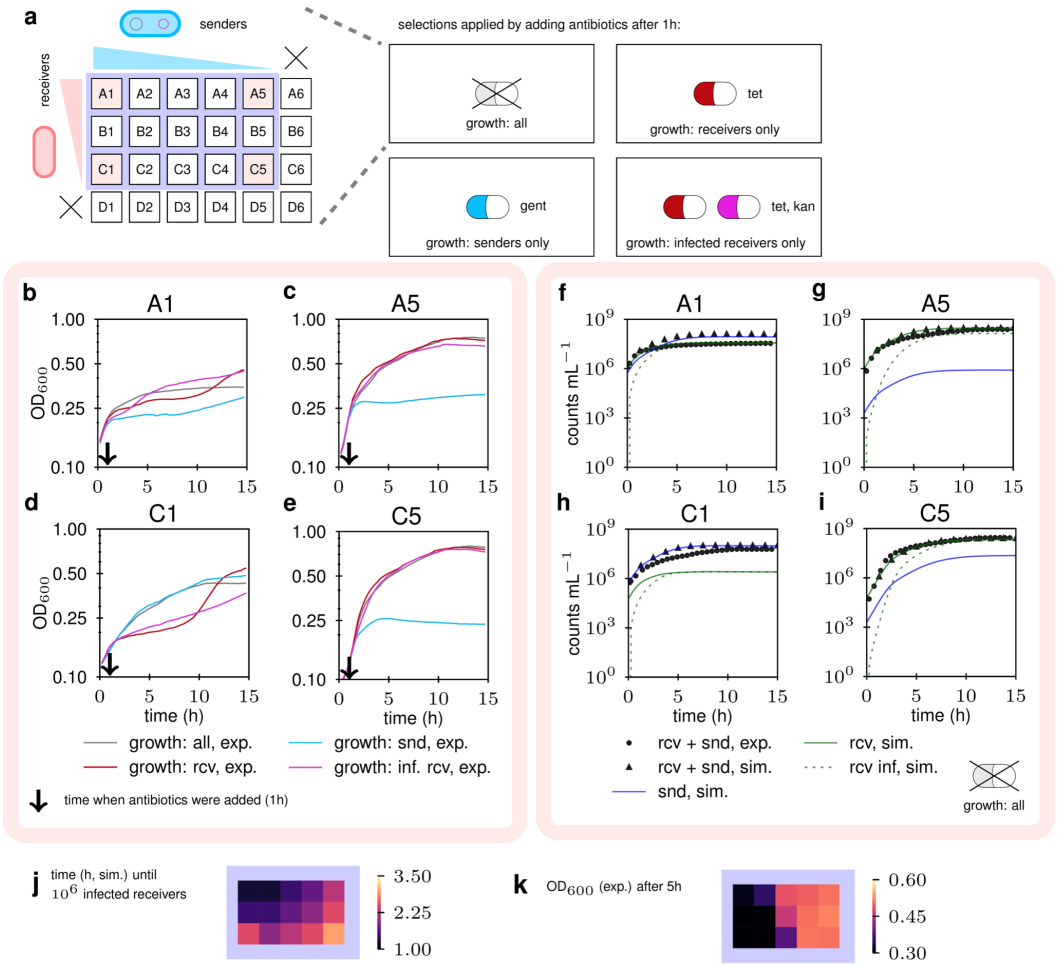

Fig. 3: Communication from senders to receivers. (a) Senders (snd) and receivers (rcv) were mixed in different combinations of their starting ODs and grown for 15h (in four sets), with different antibiotic selections applied to three sets after 1h (**Methods**). For each set, initial sender (x-axis) and receiver densities (y-axis) were varied, starting from the undiluted (OD_{600} = 0.136), in dilution steps of ½, with the last column/row having no receiver/sender. The four sets correspond to: no antibiotics added, tetracycline added to select for receivers only, gentamycin added to select for senders only, and tetracycline+kanamycin added to select for infected receivers only. **(b-e)** OD_{600} over 15h was obtained from a plate reader run (n = 1). Four representative wells are shown with the time-point of antibiotic addition indicated by an arrow. Each well shows curves for all four sets of antibiotic selection. Plots for all wells are shown in **Fig. S18**. **(f-i)** Converted cell densities (rcv+snd, exp.) are shown with deterministic simulations of the combined sender and receiver CRN model (**Note S8**) for the settings (b) to (e). For the simulations, total cell (rcv+snd, sim.), sender (snd, sim.), receiver (rcv, sim.), and infected receivers (rcv inf, sim.) concentrations are shown. As before, plots for all wells are shown in **Fig. S17** and **S19** to **S22**. **(j)** Heatmap for the purple area of (a) with simulated time (h) until the concentration of infected receivers reaches 10^6 mL^{-1} in the absence of antibiotics. The earliest time is reached with high densities of both senders and receivers (top-left). **(k)** Heatmap for the purple area of (a) with experimentally measured OD_{600} after 5h in the absence of antibiotics. Higher ODs are obtained with low initial sender densities (right).

Conditioned media inhibits phage infections

We wondered how the infection dynamics would be affected by the state of the media in long-term experiments, e.g., because of spent media reducing the growth differences between uninfected and infected cells. We collected conditioned media from senders (TOP10_H_KanΦ, containing Helper+KanΦ, Table S1) and empty-vector control cells (TOP10_Gx_Kx, Table S1), and removed cells with a 0.22 μm filter (Methods). The filtrate and phages with a different antibiotic resistance (AmpΦ) were then added to receiver cells (ER2738) prior to monitoring their growth. Fig. 4a shows plate reader data when selecting for infected receivers with ampicillin. In contrast to controls with fresh LB media and conditioned media from empty-vector control cells, a delayed growth was observed in the conditioned

media from senders. To exclude infection competition by KanR-carrying phages, they were removed from the sender conditioned media by passing through a 50kDa filter (fraction B, Fig. 4c, Methods). Infection assays with fraction B of the sender conditioned media also showed delayed growth, although a little earlier than fraction A (Fig. 4b).

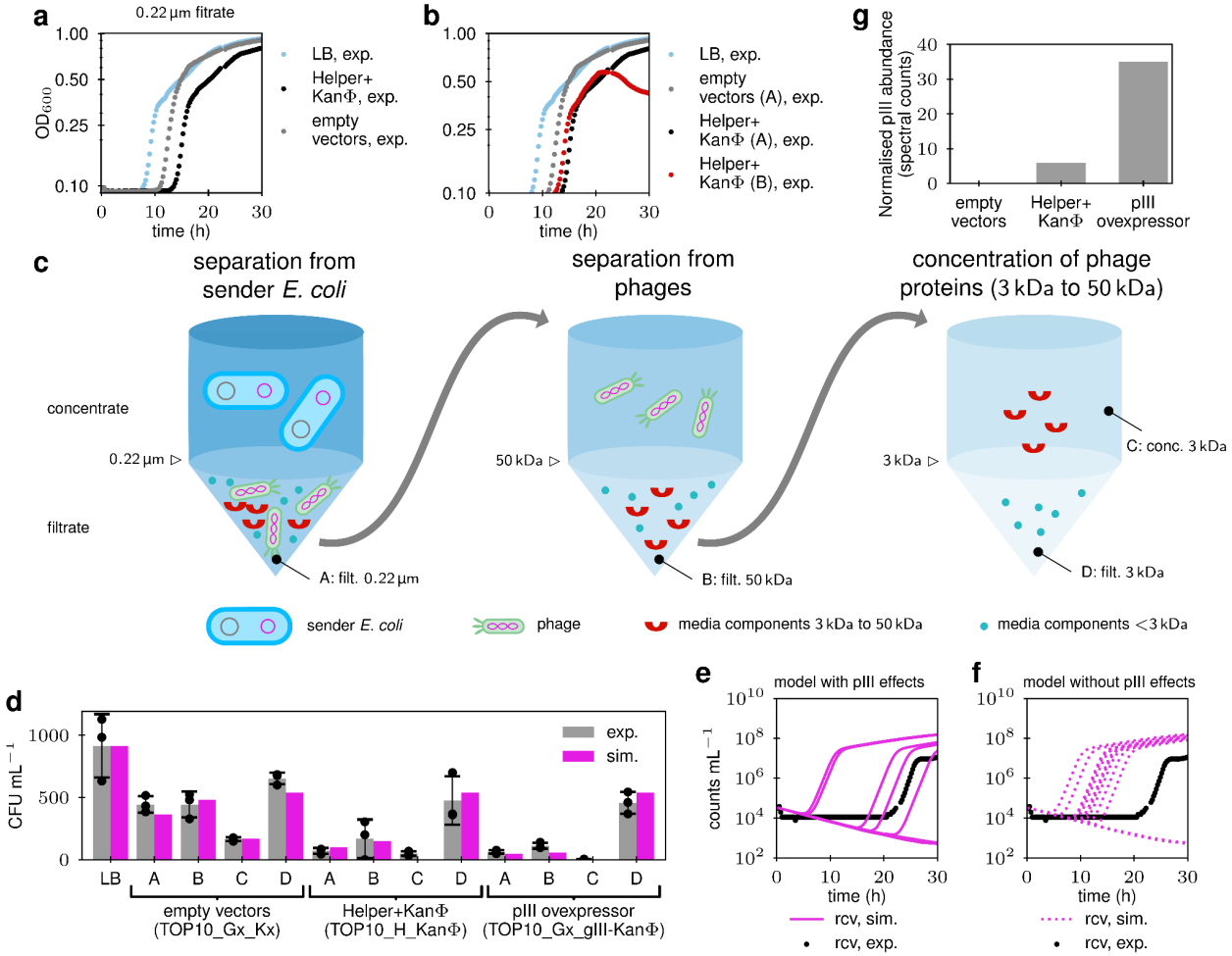

Fig. 4: Evidence for extracellular secretion of M13 gene III protein (pIII) and its inhibitory effect on infection. (a) Conditioned media from sender cells (TOP10_H_KanΦ, carrying Helper+KanΦ) and cells carrying empty vectors (TOP10_Gx_Kx) were filtered to remove the cells. The two conditioned media (48% concentration) and an LB control were then mixed with AmpΦ phages, incubated with receiver cells for infection, and the infection reactions transferred to fresh LB+ampicillin (**Methods**). Receiver growth (OD_{600}) over 30h from the three infection reactions is shown (n = 1). Plate reader runs of growth from other infections in conditioned media, and their dilutions, are shown in **Fig. S23**, both with and without ampicillin selection. **(b)** Data from (a), but in addition with sender conditioned media (fraction B) after passing through a 50kDa filter to remove KanΦ phages (48% concentration) (n = 1, see **Methods** and **Fig. S23** for additional growth data). **(c)** Preparation of filtrates (A, B, and D) and concentrate (C) by passing conditioned media through 0.22 µm, 50kDa, and 3kDa filters (**Methods**). **(d)** Subsequent infection assays of receiver cells with AmpΦ phages were carried out in an LB control and fractions A to D of three conditioned media (n = 3, see **Methods**). Data (black dots), mean (grey bars), and SD (black caps) are shown for LB and conditioned media fractions A to D from three cell cultures (TOP10_Gx_Kx, TOP10_H_KanΦ, and TOP10_Gx_gIII-KanΦ, Table S1; volumes of the fractions in **Table S3**). Simulations of our mathematical model for inhibition of infection by pIII in the conditioned medium are shown in pink (see **Note S7** for the model). **(e-f)** Receiver growth over 30h (black) with ampicillin selection (details in **Fig. S23**), following infection in fraction B of the conditioned media (80% concentration) from sender cells (TOP10_H_KanΦ). Stochastic simulations (n = 16) of receiver densities during growth, obtained from our CRN model with infection inhibition by pIII (**Note S8**), are shown (rcv, sim.) in (e) for the full model, and in (f) when disregarding infection inhibition by pIII. The model in (f) incorrectly predicts too early growth, or no growth, of receiver cell densities. **(g)** pIII abundance in conditioned media from the three cell cultures, as determined by secretome analysis by liquid chromatography with tandem mass spectrometry (LC-MS/MS) (**Methods**).

Intrigued by the above results, we next performed a CFU assay to quantify the number of phages when the infection is carried out in different conditioned media fractions (Fig. 4c). We find that fractions A, B, and C of conditioned media from TOP10_H_KanΦ cells (with helper and phage) reduce the number of infected colonies by 92%, 82%, and 94% compared to the LB control, respectively, while infected colonies in fraction D are only reduced by 48% (Fig. 4d). This indicates that a component present in fractions A, B, and C of the sender medium, but absent in fraction D, is causing the infection inhibition. It follows that this component is between 3 and 50 kDa in size (with all M13 proteins being within 3kDa to 47kDa) and is uniquely present in the conditioned media from the senders, but not from the parental strain. In this CFU assay, although the infection takes place in the conditioned media fractions, growth occurs on fresh LBA plates, ruling out any growth effects on growing cells after plating on LBA. Taken together with data from control conditioned media, the reason for reduced infection efficiency in the sender conditioned media appears to be a sender-specific molecule in its secretome (fraction A, Fig. 4d) that reduces the percentage of successfully infecting phages in the population from 5% to 0.8%.

There are examples of superinfection inhibition where an intracellular bacteriophage protein does not allow new phage infections[49,50]. In fact, gIII expression from the M13 bacteriophage is known to prevent the entry of a new phage into its host[51,52], a result that we were able to confirm (Fig. S24). In all these examples, infection immunity is caused by intracellular phage proteins. Other reports have recently found that bacteriophages of *Bacillus* sp employ peptide-based extracellular signalling for quorum sensing for lytic-to-lysogenic switch[53,54]. We wondered if M13 encodes an extracellular factor that causes infection immunity against itself. Adding purified M13 pIII protein to the extracellular medium inhibits conjugation in *E. coli* by blocking the F-pilus[55]. Given that the F-pilus is also the surface receptor for M13 entry[56], we hypothesised that the mystery factor causing extracellular infection immunity in our experiments is pIII. To test this hypothesis, we constructed a strain that encodes pIII for overexpression in *E. coli* TOP10 cells (TOP10_Gx_gIII-KanΦ), but no other M13 phage protein. Indeed conditioned media from the pIII expresser strain showed a similar infection inhibition effect, as the conditioned media from the sender, for both the plate reader (Fig. S23) and CFU assay experiments (Fig. 4d). To directly test if the pIII protein is indeed present in the conditioned media, we sent fraction C from all the three strains (parental, sender, and pIII expressor) for mass-spectrometric analysis (Methods, Fig. 4g). The results show that pIII is present in the conditioned media prepared from the sender and the pIII overexpressor cells, but not from the control cells, confirming pIII as the extracellular factor responsible for M13 infection immunity.

We modelled the CFU assay data (Fig. 4d) with a simplified first-order kinetics infection model (Note S7). The infection rate is modulated by viscosity factors ($visc$, for A to D) and pIII concentration factors ($pIII$) that reduce the concentration of susceptible receivers to R_S, with exponential dependence on $pIII$ (first-order kinetics). The predicted CFU count (CFU) is then obtained as $CFU = P_0\left(1 - e^{-R_S \cdot rate \cdot 20min}\right)$ with $rate$ being inversely proportional to the viscosity (Stokes-Einstein) and P_0 being the initial concentration of phages. After including these factors, simulations from the model fit the data well (Fig. 4d). We found a significant reduction in infectability of cells (Methods) in fractions A from the backbone control and the full phagemid conditioned media ($p = 0.0058$), but no significant difference when comparing infectability between fractions A from the full phagemid and the

pIII overexpressor conditioned media (p = 0.6406). The calculated infection rates are reduced by 70% when going from the empty-vector control to the sender conditioned media. To evaluate the models with and without pIII inhibition, we compared the experimental data from the conditioned media fraction A against both models. We found a significant difference in the model where the pIII effect is absent (p = 0.0151 for empty vectors, 0.0918 for full phagemid, 0.0040 for pIII overexpressor) but not in the one where it is present (p = 0.1689, 0.1723, and 0.1856).

A dynamic model was obtained from the receiver model (Note S8), comprising a pIII jamming reaction for unjammed receivers (mass-action kinetics), and an unjamming reaction (first-order kinetics) for jammed receivers. Unjamming occurs upon cell duplication in one of the two daughter cells. The best fittings (Fig. 4e) were obtained with a single daughter cell becoming unjammed upon growth with resource R_2. A control model where pIII secretion is removed does not fit the experimental data (Fig. 4f), predicting a too early growth of infected receivers.

Extracellular infection inhibition is advantageous for both *E. coli* and M13

Bacteria and phages are perpetually engaged in an arms race, where they try to gain fitness advantage over each other[57]. Having discovered that the M13 minor coat protein pIII secreted by infected cells blocks the entry of M13 phage into uninfected *E. coli* cells, we decided to use our CRN model to ask whether this mechanism benefits *E. coli* or M13 in the gut environment. We simulated the gut environment as a continuous culture system where resources R_1 and R_2 flow in, and bacteria (*E. coli* and a competitor), phage M13, secreted pIII, and the resources flow out. The in- and matched out-volume basal flow-rate (R) was set around 5 mL min^{-1}, as found in literature[58–60]. *E. coli* and competitor cells flow at a rate lower by a factor (f) due to adhesion to the intestinal mucus[61] (Fig. 5a). The resources are consumed by the *E. coli* to grow and, if infected, the *E. coli* produce phages and secrete pIII. The competitor cells feed on the same resources R_1 and R_2 and have a growth rate slightly higher (+1%) than uninfected *E. coli.* Infection of *E. coli* leads to a reduced growth rate, resulting in a larger disadvantage against the competitor cells.

Our model simulations over a prolonged time (Fig. 5b, S26 to S28) show that the infection inhibition mechanism due to pIII secretion is beneficial to both *E. coli* and M13. When the *E. coli* are most sticky (f = 0.1), the resource concentration is high ($R_2 = 10^9$ mL^{-1}), and the basal flow-rates are medium (factor 2-6) (Fig. 5b), both *E. coli* (uninfected+infected) and M13 (inside+outside cells) numbers are 4-6 orders of magnitude higher than would be expected without pIII secretion. In these settings, and for a given secreted pIII concentration, as the basal flow-rate increases the *E. coli* numbers reduce slightly but the M13 numbers reduce quite dramatically. This indicates that at higher basal flow-rates, the relative advantage of pIII secretion for M13 is much higher than that for *E. coli*. When the *E. coli* are less sticky (f = 1), the pIII secretion advantage still exists, but quickly diminishes with increasing basal flow-rate. In Fig. 5b, the pIII secretion rate was varied from 0.1 to 10^5 times the nominal rate and found to benefit M13 over a large range, except at an unrealistically high rate where it leads to washout.

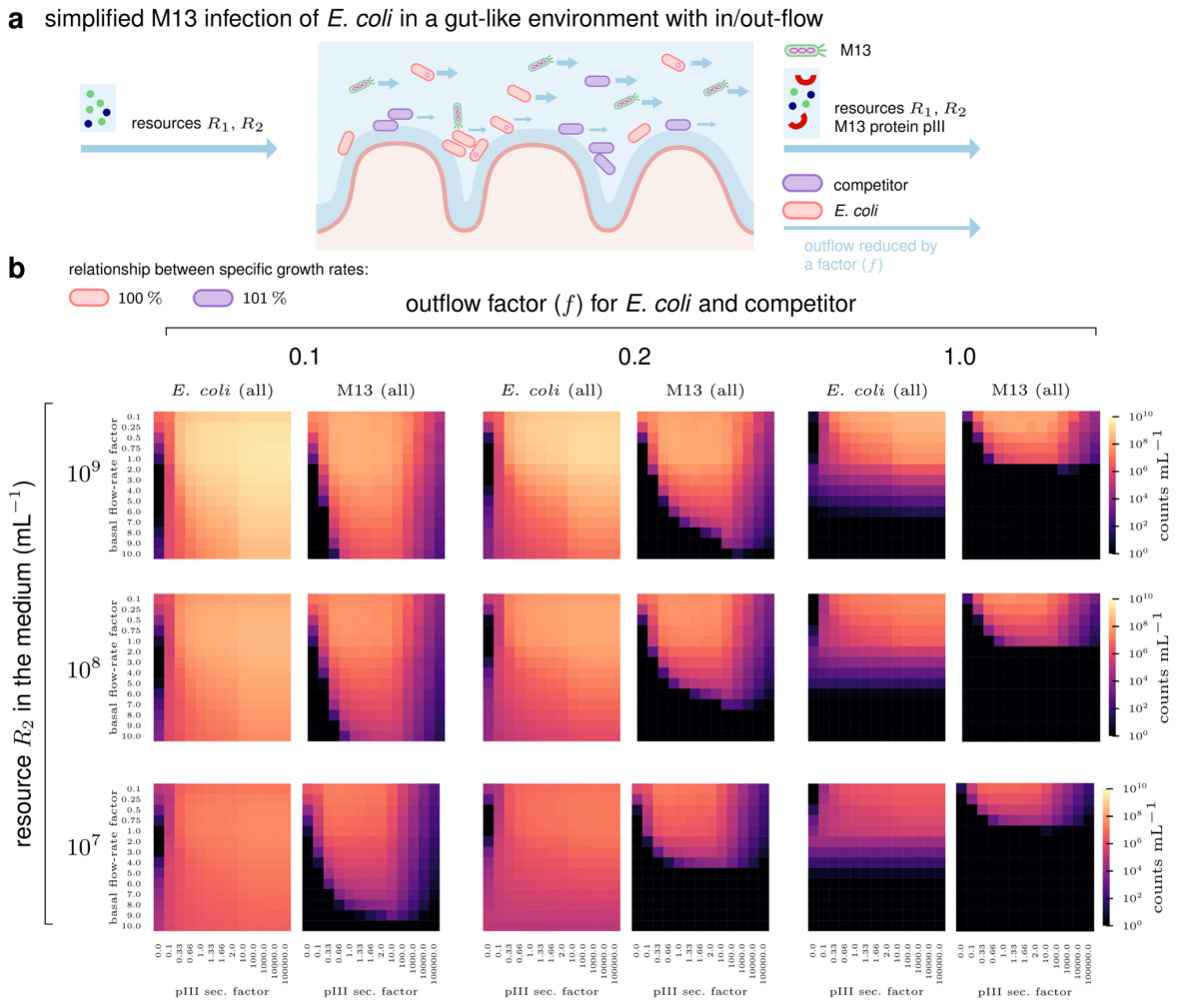

Fig. 5: Simulation of long-term infection with and without self-jamming of M13 phages. (a) A simple CRN model (**Note S8**) for M13 in a gut-like environment that combines secretion and infection capabilities from the sender and receiver models into a single *E. coli* host (red), feeding on resources R_1 and R_2. A competitor cell (blue) is assumed to feed on the same resources. The gut-like environment is modelled by an in-flow of resources and a matched out-flow of resources, M13, protein pIII, and *E. coli* and competitor cells. The *E. coli* and the competitor flow out at a rate reduced by the outflow factor f due to adhesion to the gut mucus. **(b)** Simulations for the case where the competitor cell has a specific growth rate 1% higher than the uninfected *E. coli* (for different choices see **Fig. S30** & **S31**). Counts mL^{-1} of all *E. coli* (infected and uninfected) and all M13 phages (inside and outside cells) after 40d are shown in each heatmap tile for varying relative basal flow-rates (rows = inner y-axis, 1 = 5 mL min^{-1}) and varying pIII secretion rates (columns = inner x-axis). The tile column with pIII secretion factor 0 corresponds to the case without infection inhibition via pIII. The heatmap tiles in turn are organised according to varying resource R_2 concentrations (outer y-axis) and varying outflow factors f (outer x-axis). The initial concentration of *E. coli* (with a high infectability fraction of 10%) and the competitor cells is 10^3 mL^{-1} (changes up to 10^5 mL^{-1} showed no visible difference).

Fig. S26 to S28 show how pIII secretion ensures higher *E. coli* and M13 concentrations in the presence of competitor cells by maintaining a sub-population of jammed, and hence uninfectable, fast-growing receivers. *E. coli* inhibited by pIII have growth rates close to the competitor's and constantly replenish infectable receivers, ensuring that M13 are not washed out. Fig. S29 shows a control simulation without pIII secretion. We also varied the competitive pressure on the *E. coli* by setting the growth rate of the competitors equal to uninfected *E. coli* (Fig. S30) and 5% higher (Fig. S31). We found that the pIII advantage is more pronounced against a faster-growing competitor: compare, e.g., the bottom-left tile where the range of flow rates for which pIII secretion is advantageous is larger.

Discussion

Here, we have developed an intercellular communication system that uses the M13 phage machinery to package ssDNA as a signalling molecule. Unlike small-molecule based signals, by virtue of their high programmability nucleic acid signals have a higher potential for easily generating orthogonal signal variants[62,63]. With the large M13 packing capacity of 40 kb DNA[64], they are amenable to delivery of a wide range of genetic programs, from fluorescence and antibiotic markers[36] to metabolic pathways[65], toxic peptides[66] and sequence-specific antimicrobials[67]. The message latency, defined as the time until 10^6 receivers are infected, ranges from 1.25h to 3.5h in our setup (Fig. 3j). For a phagemid size of 5.6 kb we thus get an average transmission rate of 1.25 bases per second (2.5 bits per second). While this is significantly lower than the first modems (~100 bit per second[68]) it is not much lower than the intracellular information transmission rate via transcription as seen in *E. coli* (12-42 nt s^{-1})[69].

As a well-studied model filamentous phage, the kinetics of the natural M13 infection cycle have been known and modelled for decades[40,43,45,56,70,71]. In this work, we focus on modelling the kinetics of engineered phages where infection and packaging functions have been separated into different DNA molecules, with a focus on future engineering applications in cell-to-cell communication and phage therapy. Inspired by the communication primitives in networked computer systems[72,73,74], for a comprehensive and realistic description of the signalling process, our quantitative models include several features of phage communication not previously seen together: cost of maintaining the communication machinery and the received signal, growth-phase dependent differences in signalling efficiency, antibiotic effects, as well as stochasticity of events.

As it often happens in synthetic biology, attempts to engineer a system may help discover unexpected insights into it[75–77]. In our case, we discovered that conditioned media from phage producers inhibits phage infection. While superinfection immunity due to intracellular phage proteins has been reported in many systems (sieB of *Salmonella* phage P22 and *E. coli* phage lambda[49], pIII of *E. coli* phage M13[51], PfsE of *Pseudomonas* phage Pf[50]), to the best of our knowledge, this is the first example of extracellular release of a phage protein to modulate immunity against self. Although mechanistically dissimilar, it is reminiscent of immune evasion by respiratory syncytial virus mediated by its extracellular soluble G protein[78,79], suggesting that yet another mammalian immune system feature may have a prokaryotic counterpart[80]. The mechanism of pIII release into the medium is currently unknown, and will be an area of future inquiry; it is possible that pIII is secreted in outer membrane vesicles[81]. Irrespective of the exact mechanism, our data show that the pIII is present in the extracellular medium and protects uninfected *E. coli* against M13 infection, settling an open question about an unknown “diffusible factor” that was speculated upon 45 years ago based on observations from M13 cultures of different densities[82].

Bacteria and phages are perpetually engaged in a coevolutionary arms race[83,84]. In obligate parasitic relationships like these, the molecular mechanisms of one-upmanship get so intertwined during long-term association that the fitness advantage of the bacterium and the phage may get mutually aligned[85], converging in facultative mutualism[86]. This makes it harder to assess the successes of the phage parasite and the host bacterium separately, leading to suggestions that a “virocell” paradigm that sees the infected host as a different organism is a more appropriate way of assessment[87]. Here, we use three different measures

(free phages, infected cells, free phages+infected cells) to assess this (Fig. 5b, S26-S31), and found that the results hold across all measures. The self-jamming mechanism we report protects a fraction of uninfected bacteria from M13 infection, allowing them to multiply at higher rates. In turn, this makes a fresh crop of bacteria available to M13 for future infections. This resembles the host-farming[88] practices of the *Salmonella* phage P22 where a population of susceptible hosts is generated following asymmetric cell division of an infected host[89]. Our observations can have key implications for technologies like phage display and phage-assisted continuous evolution [37,39,90], and could inform future phage therapy applications such that baseline self-immunity is incorporated as a design principle to delay the emergence of resistance against therapeutic phages[91].

Methods

Bacterial strains, growth conditions, and cloning

All *Escherichia coli* strains were grown at 37 °C in LB media (liquid with shaking at 200 rpm, or solid LBA plates with 1.5% w/v agar) supplemented with the appropriate antibiotics at the following concentrations (unless otherwise indicated): kanamycin (kan 30 μg mL^{-1}), ampicillin (Amp 100 μg mL^{-1}), gentamycin (gent 10 μg mL^{-1}), tetracycline (tet 10 μg mL^{-1}), and streptomycin (Str 50 μg mL^{-1}); concentrations were halved when using dual antibiotic selection. Strains and antibiotics used are listed in Table S1. To calculate the growth rates of strains, cells were diluted 100x from overnight cultures and re-grown in a 96-well plate (200 μL per well) in a plate-reader (Biotek Synergy HTX) until they reached an OD_{600} of 0.2 to 0.3, following which they were diluted again by 40x into a new plate. Cultures in the second plate were grown overnight, recording their OD_{600} at 15 min intervals. The data generated was used to calculate the Specific Growth Rates (Fig. S7).

Cloning was performed by Golden Gate Assembly of PCR-amplified DNA fragments using NEB enzymes: Q5 DNA polymerase (#M0492), BsaI-HFv2 (#R3733), and T4 DNA ligase (#M0202M). *E. coli* strains Dh5α and TOP10 were used for cloning. All plasmids constructed were verified by Sanger sequencing. Sequences of plasmids used in this study are listed in Table S1.

Absorbance-cell density relationship

The relationships between absorbance (OD_{600}) and cell density for the two strains (Fig. S5 a&b, S6) were determined by diluting by 1000x an overnight culture and re-growing at 37 °C in fresh LB media. Aliquots were taken from the growing cultures at several time-points and their absorbance (OD_{600}, spectrophotometer) recorded, cooled down on ice for ~30 min, following which they were serially diluted, 10^{-4} to 10^{-7} dilutions were spread on LBA plates, and the colony forming units (CFU) obtained were counted the next day. In a separate experiment (Fig. S4), the relationship between the absorbance measured using a spectrophotometer (UVisco V-1100D) and a plate-reader (Biotek Synergy HTX) was determined, and the relationship with cell density accordingly re-determined (S5 c&d).

Phage secretion

To determine the effect of cell physiology on phage secretion, three independent cultures of sender cells (TOP10_H_KanΦ) were grown in shaker flasks to different cell densities (spectrophotometer OD_{600} ~ 0.05, 0.1, 0.2, 0.3, 0.4, 0.6, 1.0, 1.5, 2) from 1000x diluted overnight cultures, 1 mL each of the cultures was spun down at 4000x g, the supernatant filtered using a 0.22 μm filter, and the filtrate (phage prep) saved at 4 ˚C. Subsequently, the receiver strain (ER2738) was grown to OD_{600} ~1 and used to perform the CFU assay to determine the titres in the phage preps obtained above. Phage preps from other sender cells (TOP10_H_AmpΦ) were similarly prepared from an overnight grown culture and quantified using the CFU assay. Preps from sender cells that produce plaque-forming phages (TOP10_H_gIII-KanΦ, TOP10_HΔgIII_gIII-KanΦ) were quantified using the CFU assay (receiver: ER2738 or ER2738_HΔgIII) and/or the PFU assay (receiver: ER2738_HΔgIII).

Phage infection, and CFU/ PFU assays

Phage titres were quantified using either a CFU or a PFU assay. Both assays involve mixing a phage dilution with *E. coli* receiver cells (containing an F-plasmid) followed by: either (1) a period of incubation and then spreading onto a selective LBA plate (CFU assay), or (2) immediate mixing with soft agar and pouring on a solid LBA plate (PFU assay).

For the CFU assay, receiver cells grown overnight were diluted 1000x and re-grown at 37 °C in LB (with appropriate antibiotics) until they reached a spectrophotometer OD_{600} between 1 and 1.5. Cells were chilled on ice for at least 30 min, and then 90 µL aliquoted into eppendorf tubes. The tubes were moved to room temperature (RT) for 5 min before adding phages to the cells. 10 µL of different phage dilutions (10^{-1} to 10^{-7}) were mixed with the receiver cells and incubated at RT for 20 min. Thereafter, the mixtures were plated on LBA plates with the appropriate antibiotic concentration. Colonies on the LBA plates were counted the next day after incubation at 37 °C for ~16h. Counts from plates between 30 and 300 colonies were used to determine the mL^{-1} titres of the phage preps according to the formula: CFU count / (phage dilution * phage volume used in mL). Since the CFU assay relies on the ability of the phage to confer antibiotic resistance to an infected receiver cell, it can be used to quantify any phage in this study using any of the receiver cells (Table S1). For the experiments in Fig. 1 (g&i), the receivers were harvested at OD_{600} ~1 and cooled, and their density was later adjusted to different OD_{600} values (0.05, 0.1, 0.5, 1.0 and 2.5). For the experiments in Fig. 1 (h&j), the receivers were harvested at the different OD_{600} indicated and cooled, and their density later adjusted to OD_{600} of 0.5.

For the PFU assay, receiver cells (ER2738_HΔgIII) grown overnight were diluted 1000x and re-grown at 37 °C in LB (tet+gent) until they reached a spectrophotometer OD_{600} between 1 and 1.5. Cells were chilled on ice for at least 30 min, and then 90 µL aliquoted into eppendorf tubes. The tubes were moved to RT shortly before mixing 10 µL of different phage dilutions (10^{-1} to 10^{-7}) with the receiver cells, and then adding the mix to 10 mL of soft LBA (0.75% w/v agar), previously aliquoted into a 15 mL tube and kept molten at 50 °C. The phage+receiver mix in the soft agar was immediately poured onto a solid plate with 20 mL hard LBA (1.5% w/v agar) with 0.2 mM IPTG and 40 µg mL^{-1} X-gal, and after the soft LBA had solidified the plate was incubated at 37 °C for 16-24h. Plaques of the non-lytic M13 phage are turbid/ diffused, usually making them harder to see. IPTG and X-gal in the hard LBA colours the plaques blue (LacZω in the F-plasmid is complemented by the LacZα in the phagemid), making them easier to visualise (Fig. S15). Counts from plates between 30 and 300 plaques were used to determine the mL^{-1} titres of the phage preps according to the formula: PFU count / (phage dilution * phage volume used in mL). Since the PFU assay relies on the phage infecting a receiver cell and getting re-secreted to infect the neighbouring receiver cells in the soft agar, it can only be used to quantify phages carrying gIII (pSB1K3_M13ps_LacZα_gIII) that infect receivers containing an M13 Helper plasmid without gIII (ER2738_HΔgIII) (see Table S1).

To determine the relationship between CFU and PFU titres obtained from the same phage prep (pSB1K3_M13ps_LacZα_gIII), three independent colonies of receiver cells (ER2738_HΔgIII) were grown to a spectrophotometer OD_{600} of 1-1.5 in LB (tet+gent) and used for both the CFU and the PFU assays (see Note S5 and Fig. S16).

Monitoring of growth and infection in a plate-reader

For the infection plate run experiments of Fig. 2, overnight cultures of receiver cells (ER2738) were diluted 1000x and re-grown to a spectrophotometer OD_{600} of 0.6-0.7, following which they were cooled on ice for ~30 min and their OD_{600} re-adjusted to different densities (0.25, 0.125, 0.0625. 0.03125) while still on ice. Several serial dilutions (3^N-fold, N = 0 to 10) of the phage prep (pSB1K3_M13ps_LacZα_gIII, undiluted concentration of $36.2x10^5$ PFU mL^{-1}), and a no-phage control, were prepared and 45 µL aliquoted into a 96-well plate at RT. 150 µL of the different receiver dilutions were added to the plate and incubated at RT for 20 min. Next, 5 µL of LB was added to each well, without or with kanamycin (end concentration 30 µg mL^{-1}), and the plate grown overnight while recording OD_{600} at 15 min intervals. The above experiments were repeated four times, each with a different set of phage dilutions added to the plate: (a) 3x technical replicates of dilutions 3^8-3^{10} and the no-phage control (continuous), (b) 3x technical replicates of dilutions 3^1-3^3 and the no-phage control (continuous), (c) 3x technical replicates of dilutions 3^1-3^3 and the no-phage control (discontinuous), and (d) single replicate of dilutions 3^0-3^{10} and the no-phage control (continuous). All data from the four repeats were combined before plotting/ model-fitting. In the discontinuous run, the plate was paused at several time-points (0, 2, 6, and 10h) to draw a 3 µL sample from each well of the third column (phage dilution 3^2), which was added to 200 µL of LB (gent) to kill all cells and later used to quantify by PFU assay the unadsorbed phages in the well (Fig. 2c). The pauses for phage sampling resulted in an average gap of ~45 min between plate reader measurements before and after the pause, resulting in the plotted time-points in Fig. 2c being accordingly delayed.

For the communication plate run experiments of Fig. 3, an overnight culture of receiver cells (ER2738) was diluted 10000x and re-grown to a spectrophotometer OD_{600} of 0.4, following which it was cooled on ice for ~30 min and several OD_{600} dilutions made (0.136, 0.068, 0.034, and 0.0) while still on ice. Overnight culture of senders (TOP10_H_gIII-KanΦ) was diluted 100x and re-grown to a spectrophotometer OD_{600} of 0.2, following which it was cooled on ice for ~30 min and several OD_{600} dilutions made (0.136, 0.068, 0.034, 0.017, 0.0085, and 0.0) while still on ice. 90 µL of receiver cell dilutions were added per well to a 96-well plate in quadruplet (see Fig. 3a for the organisation of the four sets), followed by 90 µL of the sender cell dilutions also in quadruplet. The plate was run at 37 ºC for 1h, following which 20 µL of LB with the appropriate antibiotics (5x concentrated, to achieve the standard end-concentration) was added to each well, and the plate was grown overnight while recording OD_{600} at 15 min intervals.

Phage infections in the conditioned media fractions

Cultures of six strains (see Fig. S23, Table S1) were grown overnight in LB (gent+kan), spun down at 4000x g, the supernatant filtered using a 0.22 µm filter (Millipore SLGP033RS) to remove any cells, and the filtrate saved at 4 ºC (fraction A, conditioned media). Of these strains, since TOP10_H_KanΦ is the only one expected to produce phages, conditioned media (fraction A) from it was also filtered using a 50 kDa filter (Millipore UFC905024) to obtain phage-free conditioned media (fraction B). Six concentrations (0% = fresh LB control, 16%, 32%, 48%, 64%, and 80%) of these conditioned media were used as background to run plate-reader infection experiments (as above) using an AmpΦ phage (pSEVA19_M13ps). Briefly, 160 µL of the six media dilutions prepared

earlier from each of the seven media types (fraction A from six different strains as well as fraction B from TOP10_H_KanΦ) were added to a 96-well plate, followed by 20 µL of the AmpΦ phage (undiluted concentration $1.85x10^4$ CFU mL^{-1}). Finally, 20 µL of ER2738 receivers (grown to a mid-log phase and resuspended to OD_{600} of 2.6) were added to each well (effective OD_{600} of 0.26) and incubated at RT for 20 min. Following the incubation, 10 µL of the above infection reactions were added to a new 96-well plate containing fresh LB (without and with 100 µg mL^{-1} ampicillin), and the plate grown overnight while recording OD_{600} at 15 min intervals. The data are plotted in Fig. 4a-b, 4e-f, and S23.

200 mL cultures of a subset of the strains used above (TOP10_H_KanΦ, TOP10_Gx_Kx, and TOP10_Gx_gIII-KanΦ, Table S1) were grown overnight in LB (gent+kan). Each culture was spun down at 4000x g, the supernatant filtered using a 0.22 µm filter (Millipore S2GPU05RE) to remove any cells, and the filtrate saved at 4 ºC (fraction A, phage prep). 15 mL of fraction A was filtered again using a 50 kDa filter (Millipore UFC905024) to remove any phages, and the ~14.8 mL filtrate saved (fraction B, secretome without phages). ~7.8 mL of fraction B was filtered again using a 3 kDa filter (Millipore UFC900324) to separate proteins larger and smaller than 3 kDa, and both the concentrate (fraction C, >3 kDa, ~600 µL each) and the filtrate (fraction D, <3 kDa, ~7 mL each) were saved (see Fig. 4c). The volumes of the fractions from each culture, listed in Table S3, were used to estimate the viscosity of the fractions (see Note S7). All four conditioned media fractions from the three strains were used as background to do a phage infection CFU assay using the AmpΦ phage. Briefly, 84 µL of the conditioned media fraction was mixed with 18.7 µL of the AmpΦ phage (undiluted concentration $8.8x10^3$ CFU mL^{-1}) at RT, followed by adding 84 µL of ER2738 receivers (previously grown to a spectrophotometer OD_{600} of 2.2 and cooled down) and incubation at RT for 20 min. Next, 50 µL (26.7%) of the above infection reactions were diluted in 150 µL fresh LB and spread on LBA plates (200 µg mL^{-1} ampicillin) that were incubated at 37 ºC overnight and the colonies counted the next day (Fig. 4d).

Effect of intracellular gIII in receivers on phage infections

Three colonies each of four receiver strains (ER2738, ER2738_HΔgIII, ER2738_H, ER2738_gIII-KanΦ) were grown to spectrophotometer OD_{600} of 1-1.3, cooled down and used for CFU assays using the AmpΦ phage (pSEVA19_M13ps, $1.85x10^4$ CFU mL^{-1}), as described previously (90 µL cells + 10 µL phage prep). Colonies were counted the next day (Table S3) and plotted (Fig. S24).

Secretome analysis

Protein content in the conditioned media fractions C from above (strains TOP10_H_KanΦ, TOP10_Gx_Kx, and TOP10_Gx_gIII-KanΦ) was quantified using Bradford assay (26, 26, and 32 ng $µL^{-1}$, respectively), concentrated from 250 µL to ~50 µL using a SpeedVac (Thermo Savant DNA120), and sent for shotgun proteomics analysis to the PAPPSO platform (http://pappso.inrae.fr/en/). At PAPPSO, 7.5 µL (~1 µg) each of the samples was short run on an SDS-PAGE and excised. In-gel trypsin digestion was performed on the excised gel-bands from the SDS-PAGE, and the peptides extracted and analysed by LC-MS/MS according to the platform's protocol[92], adapted for the NanoElute system. The MS/MS spectra obtained were searched against NCBI databases (*Enterobacteria phage* NC_003287.2 and *Escherichia coli* NC_000913.3) using

X!TandemPipeline (version 0.4.18)[93], the open search engine developed by PAPPSO (http://pappso.inrae.fr/en/bioinfo/xtandempipeline/). Precursor mass tolerance was 20 ppm and fragment mass tolerance was 0.02. Data filtering was achieved according to a peptide E-value < 0.01, protein E-value < 10e-4, and to a minimum of two identified peptides per protein. Sample from TOP10_Gx_gIII-KanΦ had more proteins (494) detected than from TOP10_H_KanΦ (214) or TOP10_Gx_Kx (196). The normalised abundance (expressed as spectral counts) of each protein was determined per sample. The relative abundance for M13 pIII is plotted in Fig. 4g.

Statistical Tests

We determined whether different conditioned media led to significantly different experimental outcomes (Fig. 4d). To compare two experimental outcomes (CFU counts) with each other, we used Welch's t-test. To compare experimental outcomes to model predictions, we used the Student t-test. Statistical tests were performed in Python (version 3.9.10) using the scipy.stats library (scipy version 1.5.4).

Modelling

We summarise here the main modelling decisions. For a detailed discussion of the model, we refer the reader to **Note S8** in the supplementary material.

Conversion between OD_{600} measurements of the 96-well plate reader and the spectrophotometer was performed by linear regression (Python 3.9.10, sklearn toolkit version 0.24.1, see **Note S2** and **Fig. S4**). Conversion of OD_{600} measurements to cell densities for receiver and sender strains was by cubic fits (Python 3.9.10, scipy.optimize.curve_fit version 1.5.4, see **Note S2** and **Fig. S5**) of CFU counts over OD_{600} measurements.

We used chemical reaction networks (CRNs) that describe the dynamics of a system by species and reactions that act upon them (**Box S3**). The CRN models were simulated with a custom simulation framework (https://github.com/ROBACON/BCRNsim) in Python (version 3.9.10) that generates SBML models and internally runs CopasiSE (version 4.34, build 251) to obtain stochastic (by the direct method) and ODE (by the LSODA solver) simulations. Simulations were parallelized using joblib, and the simulation data was post-processed and plotted in Python. Parametrization of the initial CRN model and subsequent extensions began with a basic growth model from corresponding experimental data, which was then iterated on by adding new parameters and reactions to the model (phage secretion, infection, antibiotics, inhibition via external pIII) to fit more involved experimental setups. Fitting was done by particle swarm optimization in Python and, if needed, adjusted manually. We next summarise the iterative model build-up (for details see **Note S8**).

We resorted to a linear resource consumer model with two resources to model the experimentally observed two-phase exponential growth of senders and receivers (**Note S3**, **Box S3**, and **Fig. S8**). Starting from the growth models, we first integrated phage secretion into the sender model (**Fig. 1**). We then detailed the receiver model by adding infection kinetics **(Fig. 1f-h**). The infection model uses a reaction with first-order kinetics for infection of receivers by phages (**Fig. 1g&i**) and two infectability states with different infection rates

for a receiver (**Fig. 1h&j**). We further expanded the receiver CRN model by uptake and decay reactions induced by the antibiotics (e.g., kan). The newly introduced parameters for antibiotic uptake and death were calibrated with plate reader runs and CFU counts (**Fig. 1,** see **Methods** for experimental setup). A simplified, deterministic, first order kinetics, receiver infection ODE model was derived for the case where bacterial growth can be neglected. The simplified model was used to relate CFU and PFU counts (**Note S6**). The full CRN sender and receiver models were then combined into a single CRN to model end-to-end communication of senders to receivers, including phage secretion, infection, and immunity to different antibiotics (tet, gent, kan). The newly introduced parameters of tet and gent uptake and death were calibrated via plate reader runs (**Fig. 3**, see **Methods** for experimental setup). To model and confirm inhibition via external pIII in conditioned media, we resorted to a simplified, static first-order kinetics infection model (**Fig. 4d**). In a second step, the full receiver CRN model from **Fig. 3** was extended by inhibition via external pIII. Inhibition was assumed to follow first-order kinetics and block entry of phages. The newly introduced parameters were fitted with plate reader experiments (**Fig. 4e**, see **Methods** for experimental setup). The simplified wild-type M13 model in the gut (**Fig. 5**) was obtained by combining secretion and infection kinetics of senders and receivers (so far associated with separate cell types), allowing the same cell to have both functions. Since newly introduced additional parameters like the pIII secretion rate and the reduced out-flow rates of cells due to adhesion to the gut mucus could not be fitted with experimental data, we varied these parameters over large ranges to test for the robustness of our predictions.

Acknowledgements

We thank Jean-Loup Faulon for his support and generous access to various laboratory equipment, and Marie-Agnès Petit for access to the UVP ColonyDoc-It. We thank Alfonso Jaramillo for the kind gift of bacterial strains (TOP10, TG1, SAJ635) and plasmids (PAJ297, PAJ156), and Vijai Singh for help in constructing PAJ156. We thank Hadi Jbara, Roman Luchko, Abhinav Pujar, and Tom Zaplana for technical assistance. We thank Sayantan Bose, Alexandra Gruss, Alfonso Jaramillo, and Marie-Agnès Petit for valuable comments and discussions. We thank Lydie Oliveira Correia and Aaron Millan-Oropeza (PAPPSO) for the proteomics analyses, which were performed on the PAPPSO platform (http://pappso.inrae.fr/en/) supported by INRAE (https://www.inrae.fr/en), the Ile-de-France regional council (https://www.iledefrance.fr/education-recherche), IBiSA (https://www.ibisa.net), and CNRS (http://www.cnrs.fr). We thank the Max Planck Institute for Informatics (MPI-INF) for access to cluster computing time. We acknowledge support from the Digicosme working group HicDiesMeus, Ile-de-France (IdF) region's DIM-RFSI (project COMBACT), INS2I CNRS (project BACON), Université Paris-Saclay's STIC department (project DEPEC MODE), and INRAE's MICA department (project PHEMO). This research was funded in part by the National Research Agency (ANR) under the DREAMY project (ANR-21-CE48-0003).

Author contributions

M.F., T.N., and M.K. conceived the study.
A.Pat., and M.K. designed the wet-lab experiments.
A.Pat., C.H., A.Pan., and M.K. performed the wet-lab experiments.
C.H., M.F., and T.N. built and simulated the computational models.
A.Pat., M.F., T.N., and M.K. analysed the data.
M.F., T.N., and M.K. acquired the funding.

M.F., T.N., and M.K. wrote the manuscript with contributions from all authors.
All authors read and approved the final manuscript.

Competing interests

The authors declare no competing interests.

References

1. Shapiro, J. A. Thinking about bacterial populations as multicellular organisms. *Annu. Rev. Microbiol.* **52**, 81–104 (1998).
2. Grosberg, R. K. & Strathmann, R. R. The Evolution of Multicellularity: A Minor Major Transition? *Annu. Rev. Ecol. Evol. Syst.* **38**, 621–654 (2007).
3. Ispolatov, I., Ackermann, M. & Doebeli, M. Division of labour and the evolution of multicellularity. *Proc. Biol. Sci.* **279**, 1768–1776 (2012).
4. Tsoi, R. *et al.* Metabolic division of labor in microbial systems. *Proc. Natl. Acad. Sci. U. S. A.* **115**, 2526–2531 (2018).
5. West, S. A. & Cooper, G. A. Division of labour in microorganisms: an evolutionary perspective. *Nat. Rev. Microbiol.* **14**, 716–723 (2016).
6. Alberts, B. *et al. General Principles of Cell Communication*. (Garland Science, 2002).
7. Mittelbrunn, M. & Sánchez-Madrid, F. Intercellular communication: diverse structures for exchange of genetic information. *Nat. Rev. Mol. Cell Biol.* **13**, 328–335 (2012).
8. Mathieu, M., Martin-Jaular, L., Lavieu, G. & Théry, C. Specificities of secretion and uptake of exosomes and other extracellular vesicles for cell-to-cell communication. *Nat. Cell Biol.* **21**, 9–17 (2019).
9. Soucy, S. M., Huang, J. & Gogarten, J. P. Horizontal gene transfer: building the web of life. *Nat. Rev. Genet.* **16**, 472–482 (2015).
10. Andam, C. P., Carver, S. M. & Berthrong, S. T. Horizontal Gene Flow in Managed Ecosystems. *Annu. Rev. Ecol. Evol. Syst.* **46**, 121–143 (2015).
11. Hemme, C. L. *et al.* Lateral Gene Transfer in a Heavy Metal-Contaminated-Groundwater Microbial Community. *MBio* **7**, e02234–15 (2016).
12. Kent, A. G., Vill, A. C., Shi, Q., Satlin, M. J. & Brito, I. L. Widespread transfer of mobile antibiotic resistance genes within individual gut microbiomes revealed through bacterial Hi-C. *Nat. Commun.* **11**, 4379 (2020).
13. von Wintersdorff, C. J. H. *et al.* Dissemination of Antimicrobial Resistance in Microbial Ecosystems through Horizontal Gene Transfer. *Front. Microbiol.* **7**, 173 (2016).
14. Hehemann, J.-H. *et al.* Transfer of carbohydrate-active enzymes from marine bacteria to Japanese gut microbiota. *Nature* **464**, 908–912 (2010).

15. French, K. E., Zhou, Z. & Terry, N. Horizontal 'gene drives' harness indigenous bacteria for bioremediation. *Sci. Rep.* **10**, 15091 (2020).
16. Sweere, J. M. *et al.* Bacteriophage trigger antiviral immunity and prevent clearance of bacterial infection. *Science* **363**, (2019).
17. Hassan, F., Kamruzzaman, M., Mekalanos, J. J. & Faruque, S. M. Satellite phage TLCφ enables toxigenic conversion by CTX phage through dif site alteration. *Nature* **467**, 982–985 (2010).
18. Lee, I. P. A., Eldakar, O. T., Gogarten, J. P. & Andam, C. P. Bacterial cooperation through horizontal gene transfer. *Trends Ecol. Evol.* (2021) doi:10.1016/j.tree.2021.11.006.
19. Moon, T. S., Lou, C., Tamsir, A., Stanton, B. C. & Voigt, C. A. Genetic programs constructed from layered logic gates in single cells. *Nature* **491**, 249–253 (2012).
20. Daniel, R., Rubens, J. R., Sarpeshkar, R. & Lu, T. K. Synthetic analog computation in living cells. *Nature* **497**, 619–623 (2013).
21. Pandi, A. *et al.* Metabolic perceptrons for neural computing in biological systems. *Nat. Commun.* **10**, 3880 (2019).
22. Wang, B. & Buck, M. Customizing cell signaling using engineered genetic logic circuits. *Trends Microbiol.* **20**, 376–384 (2012).
23. Wan, X. *et al.* Cascaded amplifying circuits enable ultrasensitive cellular sensors for toxic metals. *Nat. Chem. Biol.* **15**, 540–548 (2019).
24. Courbet, A., Endy, D., Renard, E., Molina, F. & Bonnet, J. Detection of pathological biomarkers in human clinical samples via amplifying genetic switches and logic gates. *Sci. Transl. Med.* **7**, 289ra83 (2015).
25. Kemmer, C. *et al.* Self-sufficient control of urate homeostasis in mice by a synthetic circuit. *Nat. Biotechnol.* **28**, 355–360 (2010).
26. Isabella, V. M. *et al.* Development of a synthetic live bacterial therapeutic for the human metabolic disease phenylketonuria. *Nat. Biotechnol.* **36**, 857–864 (2018).
27. Tamsir, A., Tabor, J. J. & Voigt, C. A. Robust multicellular computing using genetically encoded NOR gates and chemical 'wires'. *Nature* **469**, 212–215 (2011).
28. Regot, S. *et al.* Distributed biological computation with multicellular engineered networks. *Nature* **469**, 207–211 (2011).
29. Guiziou, S., Ulliana, F., Moreau, V., Leclere, M. & Bonnet, J. An Automated Design Framework

for Multicellular Recombinase Logic. *ACS Synth. Biol.* **7**, 1406–1412 (2018).

30. Toda, S., Blauch, L. R., Tang, S. K. Y., Morsut, L. & Lim, W. A. Programming self-organizing multicellular structures with synthetic cell-cell signaling. *Science* **361**, 156–162 (2018).
31. Kylilis, N., Tuza, Z. A., Stan, G.-B. & Polizzi, K. M. Tools for engineering coordinated system behaviour in synthetic microbial consortia. *Nat. Commun.* **9**, 2677 (2018).
32. Stojanovic, M. N. & Stefanovic, D. A deoxyribozyme-based molecular automaton. *Nat. Biotechnol.* **21**, 1069–1074 (2003).
33. Joesaar, A. *et al.* DNA-based communication in populations of synthetic protocells. *Nat. Nanotechnol.* **14**, 369–378 (2019).
34. Secor, P. R. *et al.* Filamentous Bacteriophage Promote Biofilm Assembly and Function. *Cell Host Microbe* **18**, 549–559 (2015).
35. López-Igual, R., Bernal-Bayard, J., Rodríguez-Patón, A., Ghigo, J.-M. & Mazel, D. Engineered toxin-intein antimicrobials can selectively target and kill antibiotic-resistant bacteria in mixed populations. *Nat. Biotechnol.* **37**, 755–760 (2019).
36. Ortiz, M. E. & Endy, D. Engineered cell-cell communication via DNA messaging. *J. Biol. Eng.* **6**, 16 (2012).
37. Esvelt, K. M., Carlson, J. C. & Liu, D. R. A system for the continuous directed evolution of biomolecules. *Nature* **472**, 499–503 (2011).
38. Brödel, A. K., Rodrigues, R., Jaramillo, A. & Isalan, M. Accelerated evolution of a minimal 63-amino acid dual transcription factor. *Sci Adv* **6**, eaba2728 (2020).
39. Smith, G. P. & Scott, J. K. [15] Libraries of peptides and proteins displayed on filamentous phage. in *Methods in Enzymology* vol. 217 228–257 (Academic Press, 1993).
40. Smeal, S. W., Schmitt, M. A., Pereira, R. R., Prasad, A. & Fisk, J. D. Simulation of the M13 life cycle II: Investigation of the control mechanisms of M13 infection and establishment of the carrier state. *Virology* **500**, 275–284 (2017).
41. Mai-Prochnow, A. *et al.* Big things in small packages: the genetics of filamentous phage and effects on fitness of their host. *FEMS Microbiol. Rev.* **39**, 465–487 (2015).
42. Russel, M., Whirlow, H., Sun, T. P. & Webster, R. E. Low-frequency infection of F- bacteria by transducing particles of filamentous bacteriophages. *J. Bacteriol.* **170**, 5312–5316 (1988).
43. Lerner, T. J. & Model, P. The ‘steady state’ of coliphage f1: DNA synthesis late in infection.

Virology vol. 115 282–294 (1981).

44. Ploss, M. & Kuhn, A. Kinetics of filamentous phage assembly. *Phys. Biol.* **7**, 045002 (2010).
45. Smeal, S. W., Schmitt, M. A., Pereira, R. R., Prasad, A. & Fisk, J. D. Simulation of the M13 life cycle I: Assembly of a genetically-structured deterministic chemical kinetic simulation. *Virology* **500**, 259–274 (2017).
46. Ács, N., Gambino, M. & Brøndsted, L. Bacteriophage Enumeration and Detection Methods. *Front. Microbiol.* **11**, 594868 (2020).
47. Biebricher, C. K. & Düker, E. M. F and type 1 piliation of Escherichia coli. *J. Gen. Microbiol.* **130**, 951–957 (1984).
48. Tan, C. *et al.* The inoculum effect and band-pass bacterial response to periodic antibiotic treatment. *Mol. Syst. Biol.* **8**, 617 (2012).
49. Ranade, K. & Poteete, A. R. Superinfection exclusion (sieB) genes of bacteriophages P22 and lambda. *Journal of Bacteriology* vol. 175 4712–4718 (1993).
50. Schmidt, A. K. *et al.* A Filamentous Bacteriophage Protein Inhibits Type IV Pili To Prevent Superinfection of Pseudomonas aeruginosa. *MBio* e0244121 (2022).
51. Boeke, J. D., Model, P. & Zinder, N. D. Effects of bacteriophage f1 gene III protein on the host cell membrane. *Mol. Gen. Genet.* **186**, 185–192 (1982).
52. Brödel, A. K., Jaramillo, A. & Isalan, M. Intracellular directed evolution of proteins from combinatorial libraries based on conditional phage replication. *Nat. Protoc.* **12**, 1830–1843 (2017).
53. Stokar-Avihail, A., Tal, N., Erez, Z., Lopatina, A. & Sorek, R. Widespread Utilization of Peptide Communication in Phages Infecting Soil and Pathogenic Bacteria. *Cell Host Microbe* **25**, 746–755.e5 (2019).
54. Erez, Z. *et al.* Communication between viruses guides lysis-lysogeny decisions. *Nature* **541**, 488–493 (2017).
55. Lin, A. *et al.* Inhibition of bacterial conjugation by phage M13 and its protein g3p: quantitative analysis and model. *PLoS One* **6**, e19991 (2011).
56. Wan, Z. & Goddard, N. L. Competition between conjugation and M13 phage infection in Escherichia coli in the absence of selection pressure: a kinetic study. *G3* **2**, 1137–1144 (2012).
57. Safari, F. *et al.* The interaction of phages and bacteria: the co-evolutionary arms race. *Crit. Rev.*

Biotechnol. **40**, 119–137 (2020).

58. Fine, K. D., Santa Ana, C. A., Porter, J. L. & Fordtran, J. S. Effect of changing intestinal flow rate on a measurement of intestinal permeability. *Gastroenterology* **108**, 983–989 (1995).
59. Cremer, J. *et al.* Effect of flow and peristaltic mixing on bacterial growth in a gut-like channel. *Proc. Natl. Acad. Sci. U. S. A.* **113**, 11414–11419 (2016).
60. Cremer, J., Arnoldini, M. & Hwa, T. Effect of water flow and chemical environment on microbiota growth and composition in the human colon. *Proc. Natl. Acad. Sci. U. S. A.* **114**, 6438–6443 (2017).
61. Conway, T., Krogfelt, K. A. & Cohen, P. S. The Life of Commensal Escherichia coli in the Mammalian Intestine. *EcoSal Plus* **1**, (2004).
62. Nielsen, A. A. K. & Voigt, C. A. Multi-input CRISPR/Cas genetic circuits that interface host regulatory networks. *Mol. Syst. Biol.* **10**, 763 (2014).
63. Sexton, J. T. & Tabor, J. J. Multiplexing cell-cell communication. *Mol. Syst. Biol.* **16**, e9618 (2020).
64. Messing, J. M13 cloning vehicles. Their contribution to DNA sequencing. *Methods Mol. Biol.* **23**, 9–22 (1993).
65. Tao, W. *et al.* In Vitro Packaging Mediated One-Step Targeted Cloning of Natural Product Pathway. *ACS Synth. Biol.* **8**, 1991–1997 (2019).
66. Krom, R. J., Bhargava, P., Lobritz, M. A. & Collins, J. J. Engineered Phagemids for Nonlytic, Targeted Antibacterial Therapies. *Nano Lett.* **15**, 4808–4813 (2015).
67. Bikard, D. *et al.* Exploiting CRISPR-Cas nucleases to produce sequence-specific antimicrobials. *Nat. Biotechnol.* **32**, 1146–1150 (2014).
68. Pahlavan, K. & Holsinger, J. L. Voice-band data communication modems - A historical review: 1919-1988. *IEEE Commun. Mag.* **26**, 16–27 (1988).
69. Proshkin, S., Rahmouni, A. R., Mironov, A. & Nudler, E. Cooperation between translating ribosomes and RNA polymerase in transcription elongation. *Science* **328**, 504–508 (2010).
70. Tzagoloff, H. & Pratt, D. THE INITIAL STEPS IN INFECTION WITH COLIPHAGE M13. *Virology* **24**, 372–380 (1964).
71. Merriam, V. Stability of the carrier state in bacteriophage M13-infected cells. *J. Virol.* **21**, 880–888 (1977).

72. Tanenbaum, A. S. *Computer Networks*. (Prentice Hall, 2003).

73. Lynch, N. A. *Distributed Algorithms*. (Elsevier, 1996).

74. MedinaA, TaftN, SalamatianK, BhattacharyyaS & DiotC. Traffic matrix estimation. *ACM SIGCOMM Computer Communication Review* (2002) doi:10.1145/964725.633041.

75. Tan, C., Marguet, P. & You, L. Emergent bistability by a growth-modulating positive feedback circuit. *Nat. Chem. Biol.* **5**, 842–848 (2009).

76. Pósfai, G. *et al.* Emergent properties of reduced-genome Escherichia coli. *Science* **312**, 1044–1046 (2006).

77. Chen, Y., Kim, J. K., Hirning, A. J., Josić, K. & Bennett, M. R. SYNTHETIC BIOLOGY. Emergent genetic oscillations in a synthetic microbial consortium. *Science* **349**, 986–989 (2015).

78. Battles, M. B. & McLellan, J. S. Respiratory syncytial virus entry and how to block it. *Nat. Rev. Microbiol.* **17**, 233–245 (2019).

79. Bukreyev, A. *et al.* The secreted form of respiratory syncytial virus G glycoprotein helps the virus evade antibody-mediated restriction of replication by acting as an antigen decoy and through effects on Fc receptor-bearing leukocytes. *J. Virol.* **82**, 12191–12204 (2008).

80. Wein, T. & Sorek, R. Bacterial origins of human cell-autonomous innate immune mechanisms. *Nat. Rev. Immunol.* (2022) doi:10.1038/s41577-022-00705-4.

81. Henry, T. *et al.* Improved methods for producing outer membrane vesicles in Gram-negative bacteria. *Res. Microbiol.* **155**, 437–446 (2004).

82. Merriam, V. Stability of the carrier state in bacteriophage M13-infected cells. *J. Virol.* **21**, 880–888 (1977).

83. Bikard, D. & Marraffini, L. A. Innate and adaptive immunity in bacteria: mechanisms of programmed genetic variation to fight bacteriophages. *Curr. Opin. Immunol.* **24**, 15–20 (2012).

84. Hampton, H. G., Watson, B. N. J. & Fineran, P. C. The arms race between bacteria and their phage foes. *Nature* **577**, 327–336 (2020).

85. Correa, A. M. S. *et al.* Revisiting the rules of life for viruses of microorganisms. *Nat. Rev. Microbiol.* **19**, 501–513 (2021).

86. Shapiro, J. W., Williams, E. S. C. P. & Turner, P. E. Evolution of parasitism and mutualism between filamentous phage M13 and Escherichia coli. *PeerJ* **4**, e2060 (2016).

87. Forterre, P. The virocell concept and environmental microbiology. *ISME J.* **7**, 233–236 (2013).

88. Wahl, A., Battesti, A. & Ansaldi, M. Prophages in Salmonella enterica: a driving force in reshaping the genome and physiology of their bacterial host? *Mol. Microbiol.* **111**, 303–316 (2019).

89. Cenens, W., Makumi, A., Govers, S. K., Lavigne, R. & Aertsen, A. Viral Transmission Dynamics at Single-Cell Resolution Reveal Transiently Immune Subpopulations Caused by a Carrier State Association. *PLoS Genet.* **11**, e1005770 (2015).

90. Brödel, A. K., Jaramillo, A. & Isalan, M. Engineering orthogonal dual transcription factors for multi-input synthetic promoters. *Nat. Commun.* **7**, 13858 (2016).

91. Burmeister, A. R. *et al.* Pleiotropy complicates a trade-off between phage resistance and antibiotic resistance. *Proc. Natl. Acad. Sci. U. S. A.* **117**, 11207–11216 (2020).

92. Pérez-Pascual, D. *et al.* More Than Gliding: Involvement of GldD and GldG in the Virulence of Flavobacterium psychrophilum. *Frontiers in Microbiology* vol. 8 (2017).

93. Langella, O. *et al.* X!TandemPipeline: A Tool to Manage Sequence Redundancy for Protein Inference and Phosphosite Identification. *J. Proteome Res.* **16**, 494–503 (2017).